



Persistence length regulates emergent dynamics in active roller ensembles

Journal:	<i>Soft Matter</i>
Manuscript ID	SM-ART-03-2021-000363.R1
Article Type:	Paper
Date Submitted by the Author:	07-Apr-2021
Complete List of Authors:	Zhang, Bo; Argonne National Laboratory, Materials Science Division Karani, Hamid; Northwestern University, Engineering Sciences and Applied Mathematics Vlahovska, Petia; Northwestern University, Engineering Sciences and Applied Mathematics Snezhko, Alexey; Argonne National Laboratory, Materials Science Division

Cite this: DOI: 00.0000/xxxxxxxxxx

Persistence length regulates emergent dynamics in active roller ensembles[†]Bo Zhang,^{‡a} Hamid Karani,^{b,c‡} Petia M. Vlahovska,^b and Alexey Snezhko^{a*}

Received Date

Accepted Date

DOI: 00.0000/xxxxxxxxxx

Active colloidal fluids, biological and synthetic, often demonstrate complex self-organization and the emergence of collective behavior. Spontaneous formation of multiple vortices has been recently observed in a variety of active matter systems, however, the generation and tunability of the active vortices not controlled by geometrical confinement remain challenging. Here, we exploit the persistence length of individual particles in ensembles of active rollers to tune the formation of vortices and to orchestrate their characteristic sizes. We use two systems and employ two different approaches exploiting shape anisotropy or polarization memory of individual units for control of the persistence length. We characterize the dynamics of emergent multi-vortex states and reveal a direct link between the behavior of the persistence length and properties of the emergent vortices. We further demonstrate common features between the two systems including anti-ferromagnetic ordering of the neighboring vortices and active turbulent behavior with a characteristic energy cascade in the particles velocity field energy spectra. Our findings provide insights into the onset of spatiotemporal coherence in active roller systems and suggest a control knob for manipulation of dynamic self-assembly in active colloidal ensembles.

1 Introduction

Active colloids use energy from the environment to maintain complex collective dynamics and self-organization not accessible at equilibrium^{1–6}. Recently, the shape asymmetry of active particles has been used as a control parameter to enrich collective dynamics and self-organization in active colloidal systems^{7–11}. Active spinner fluids, comprised of autonomous spinning units injecting energy and angular momentum at the single particle level, represent a new class of active synthetic materials that enable unique dynamic phases and transport characteristics^{12–22}.

A prime example of active spinner fluids is a Quincke rollers ensemble that utilizes Quincke electro-rotation instability^{23,24} for propulsion. In the presence of a uniform electric field \mathbf{E} , the contrast in the electrical conductivity σ and permittivity ϵ between the particle and fluid causes mobile ions to accumulate at the

particle-fluid interface (Fig. 1a). The resulting dipole \mathbf{P} follows a relaxation dynamic:

$$\frac{\partial \mathbf{P}}{\partial t} = \Omega \times \mathbf{P} - \frac{1}{\tau_{\text{MW}}} (\mathbf{P} - \chi_e \mathbf{E}), \quad (1)$$

where τ_{MW} is the Maxwell-Wagner polarization time, which solely depends on the electrical properties of particle “p” and the hosting solution “s” (for spherical particles $\tau_{\text{MW}} = (\epsilon_p + 2\epsilon_s)/(\sigma_p + 2\sigma_s)$). χ_e is a parameter dependent on electric permittivities of the carrier fluid and the particle as well as the liquid conductivity¹³. For electric fields larger than a certain critical value, the induced dipole becomes unstable and spontaneous symmetry breaking occurs, leading to the particle rotation with a constant rate Ω with the rotation axis in the plane perpendicular to the applied electric field. When the particle is located near a surface transversal to the applied field, such rotation is converted into a translational motion \mathbf{v} parallel to the surface (see Fig. 1a). Since the electric field is normal to the surface, the electro-rotation of spherical Quincke rollers induces translational motions in random initial directions along the surface making them a perfect example of active particles.

It has been demonstrated previously that a large population of Quincke rollers self-organize into a single giant vortical structure²⁵ with spontaneously selected sense of rotation. The formation of such emergent structure relies on a presence of a confin-

^a Materials Science Division, Argonne National Laboratory, 9700 South Cass Avenue, Lemont, IL 60439, USA.

^b Engineering Sciences and Applied Mathematics, Northwestern University, Evanston, IL 60206 USA.

^c Department of Physics, Brown University, Providence, RI, 02912 USA.

[†] Electronic Supplementary Information (ESI) available: [details of any supplementary information available should be included here]. See DOI: 10.1039/cXsm00000x/

* E-mail: snezhko@anl.gov

[‡] These authors contributed equally to this work.

ing boundary that determines a characteristic scale of the vortex. While the formations of multiple vortices or vortex arrays in active systems have been previously observed in experiments and simulations^{22,26–33}, controlled formation of vortices in unconfined systems by using tunable kinematic parameters has remained a challenge and rarely been investigated experimentally²². In the present paper we explore two experimental realizations of well-localized tunable vortices emerging without the aid of geometrical confinements. By limiting the persistence length of individual active rollers, either by the use of shape anisotropy or polarization memory, we induce multiple self-organized vortices that are independent of any boundaries. We reveal that characteristic size of such vortices is directly related to the persistence length of individual active particles and could be manipulated in-situ. We show that dynamic vortices prefer anti-ferromagnetic ordering regardless of the realization methods. The similarity in collective behavior of the two systems is further extended towards an active turbulence, with both systems showing a slope of $-8/3$ in the large- k part of the particles velocity field energy spectra.

2 Experimental

In our experiments with shape anisotropic colloidal rollers we use pear-shaped polystyrene colloidal particles (G0500, Thermo Scientific) with an averaged diameter of $4.8 \mu\text{m}$. The particles are dispersed in a 0.15 mol L^{-1} Dioctyl sulfosuccinate sodium salt (AOT)/hexadecane solution with a conductivity $\sigma = 3.7 \times 10^{-8} \text{ S/m}$. The colloidal suspension is then injected into a cylindrical well with a diameter $D = 2 \text{ mm}$ assembled from two Indium-Tin-Oxide (ITO) coated glass slides (IT100, Nanocs) separated by a spacer (SU-8). The thickness of the spacer is $45 \mu\text{m}$. The system is energized by a uniform DC electric field applied perpendicular to the bottom plate of the cell, see Fig. 1a. The electric field is supplied by a function generator (Agilent 33210A, Agilent Technologies) and a power amplifier (BOP 1000M, Kepco Inc.). The dynamics of colloidal particles is observed under a microscope with a $4\times$ objective and videos are captured by a fast-speed CMOS camera (IL 5, Fastec Imaging) with a frame rate of 850 frames per second.

In the case of spherical colloidal rollers we use polystyrene spheres (Phosphorex, Inc.) with a diameter $d_s = 40 \mu\text{m}$ suspended in fluid (0.15 mol L^{-1} AOT/hexadecane solution with a conductivity $\sigma = 1.2 \times 10^{-8} \text{ S/m}$). The Maxwell-Wagner time for this system is $\tau_{\text{MW}} \sim 3.85 \text{ ms}$. The suspension of spherical colloidal particles is confined inside of a $2 \times 2 \text{ cm}^2$ rectangular chamber comprised of two ITO coated glass slides (Delta Technologies), separated by a Teflon spacer with thickness of $120 \mu\text{m}$. The particle motion and tracking is visualized using an inverted optical microscope (Zeiss) mounted on a vibration isolation table (Kinetic Systems, Inc.) and videos were recorded at frame rates higher than 1000 frames per second by a high speed camera (Photron). The system is powered by a pre-designed pulsed electric field supplied by a high voltage amplifier (Matsusada) controlled by a function generator (Agilent Technologies) with a custom waveform controlled by a Matlab code.

Particle tracking, flow field reconstruction and data analysis are carried out by means of a particle image velocimetry (PIV), par-

ticle tracking velocimetry (PTV) using open source Matlab and Python codes (PIVLab³⁴, Trackpy³⁵) as well as custom codes.

3 Control of the persistence length

The classical Quincke systems consists of spherical particles that persistently roll on a surface. At high Peclet numbers defined as $\text{Pe} = |\mathbf{v}|d^{-1}/D_{\text{rot}}$, where $|\mathbf{v}|$, d and D_{rot} are the particle linear velocity, particle diameter and the rotational diffusion, respectively, Brownian noise is not capable of altering the direction of motion and subsequently, the persistence time $\tau_p = D_{\text{rot}}^{-1}$ of particles asymptotically approaches infinity. Hence, Quincke rollers move in almost straight lines as persistent runners²⁵. The corresponding persistence length $L_p = |\mathbf{v}|\tau_p \rightarrow \infty$. In a confined domain, the persistence length of Quincke rollers becomes comparable to the characteristic length scale of the domain. As a result, only one giant vortex with characteristic length comparable to the domain size is formed in the system²⁵.

Recently, we have shown that the range of motions of the Quincke rollers can be extended (1) via controlling the polarization memory of Quincke random-walkers³², and (2) by exploiting the shape anisotropy of the rollers³³. In the later case, the persistence length L_p of particles is strongly affected by the shape anisotropy of the rollers. In contrast to spherical rollers randomly selecting axis of the rotation in the plane normal to the applied electric field, pear-shaped particles prefer rotations along the long axis due to a viscous drag anisotropy. For shape-anisotropic particle rotating under Quincke mechanism the axis of rotation is selected by a balance between polarization and viscous torques. Rotation along the short axis results in significantly high viscous drag. Furthermore, since pear-shaped particles are also asymmetric along the long axis, the axis of rotation is often tilted with respect to the long axis leading to curved rolling trajectories with curvatures depending on the field strength³³. Once in motion, two flavors of rollers are simultaneously realized: those moving with clockwise winding and rollers with counter-clockwise motion³³. The curvature of the resulting trajectories of such chiral rollers is controlled by the electric field strength. In general, the long-axis of a pear-shaped roller may have an arbitrary tilt, θ , with respect to the bottom surface of the container, and \mathbf{n} (a unit vector along the long-axis pointing toward the smaller sphere of the pear-shaped roller) can point either toward or away from the bottom surface, see Fig. 1b. The tilt angle strongly depends on the activity in the system controlled by the electric field³³. Experiments reveal, that at low field strengths (below $1.96 \text{ V}/\mu\text{m}$) corresponding to low particle velocities, the axis is tilted such that the particle orientation vector points away from the substrate ($\theta > 0$, mode α). As the activity increases with the applied field, the tilt decreases, passes through zero ($\theta = 0$, mode β) and eventually points toward the substrate ($\theta < 0$, mode γ). Variations in a tilt angle of the rollers with the electric field strength directly influence the curvature of the corresponding trajectories, and consequently, the persistence lengths of the rollers, see Fig. 1b. The persistence length of the pear-shaped rollers is defined as $L_p = |\mathbf{v}|\tau_p$, where the persistence time τ_p is the time when the velocity temporal correlation function of rollers decays to $1/e$ (See Supplementary Figure 1). The persistence length has

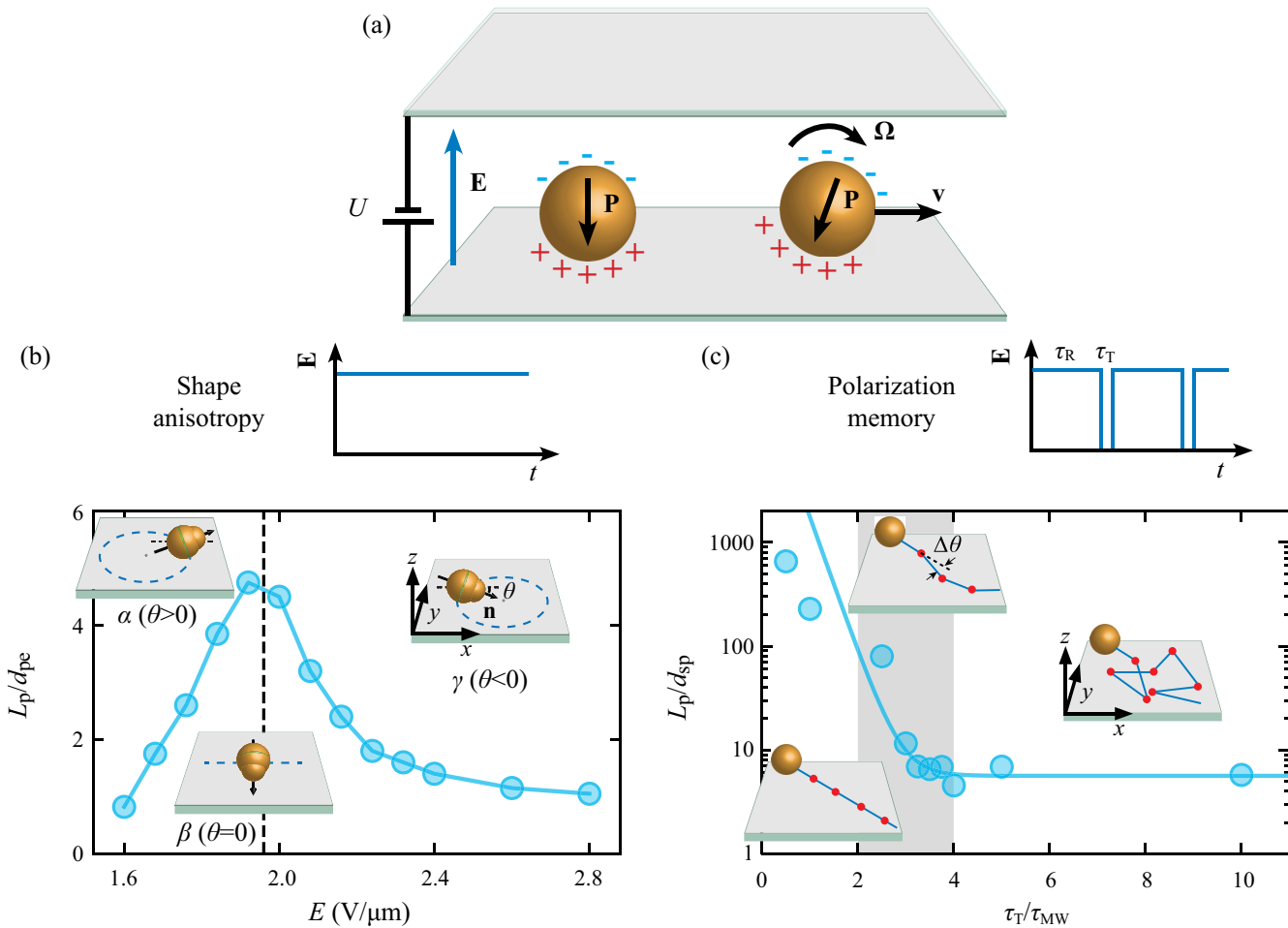


Fig. 1 Persistence lengths of Quincke rollers. (a), Sketch of Quincke rollers: static (DC) electric field induces particle polarization; above a certain threshold of the electric field a particle develops spontaneous rotation about an arbitrary axis in the plane perpendicular to the applied field. Rotations near a surface transform into a net translational motion along the bottom surface of the experimental cell. (b), Persistence length L_p of pear-shaped rollers as a function of the applied electric field strength. Depending on the field strengths, three distinctive modes of rolling can be realized illustrated by the inserts: α ("heads-out", $\theta > 0$), β ($\theta = 0$) and γ ("heads-in", $\theta < 0$). θ is the angle between the bottom plane and particle's long-axis orientation n . d_{pe} is the size of a pear-shaped particle. Blue dash lines illustrate corresponding trajectories. The black dash line indicate the crossover field where the persistence length reaches its maximum. The area fraction ϕ is 0.012. (c), Persistence length L_p of dilute spherical rollers controlled by the polarization memory τ_T/τ_{MW} by means of a pulsed electric field with a duration τ_R spaced with τ_T . Depending on τ_T/τ_{MW} ratio, a particle can perform a fully correlated random walk (left inset), partially correlated random walk (middle inset) and uncorrelated random-walk (right inset in (c)). Red dots indicate points at trajectories where the particle fully stops. d_{sp} is the diameter of a spherical particle. Shaded area represents the range of controlled parameters (τ_T/τ_{MW}) which would lead to the formation of multiple vortices.

a non-monotonic dependence on the field strength and reaches its maximum when rollers move in β mode (black dash line in Fig. 1b).

In the case of spherical rollers, the degree of the polarization memory is used to control the persistence length of individual Quincke rollers. When rectangular electric pulses with duration τ_R spaced by τ_T are applied to a spherical Quincke roller, the particle undergoes a general correlated random-walk with different degrees of directional correlation (Fig. 1c)³². When the rest time τ_T is sufficiently longer than the polarization time τ_{MW} the particle completely depolarizes during τ_T and the roller performs a fully decorrelated random walk (right inset in Fig. 1c). The corresponding persistence length is equal to the run length of the particle, i.e. $L_p = |\mathbf{v}|\tau_R$ (See more details in Supplementary Note 1). On the other end of the spectrum, for $\tau_T/\tau_{MW} < 2$, due to only

partial depolarization the particle retains its directional memory. Accordingly, the persistence length asymptotically approaches infinity, similar to persistent spherical rollers under constant DC field. However, for intermediate values of $2 \leq \tau_T/\tau_{MW} \leq 4$, the particle keeps remembering its direction of motion and performs a partially correlated random-walk³².

4 Results and discussion

Both experimental systems allow smooth and reversible in-situ manipulation of the persistence length of the particles comprising the active colloidal ensembles. While mechanisms involved in the persistence length control are different, the dynamic response of both active fluids demonstrate striking similarities. Both introduced systems exhibit rich phase behavior of the emergent dynamic states when energized by the electric field^{32,33} and sup-

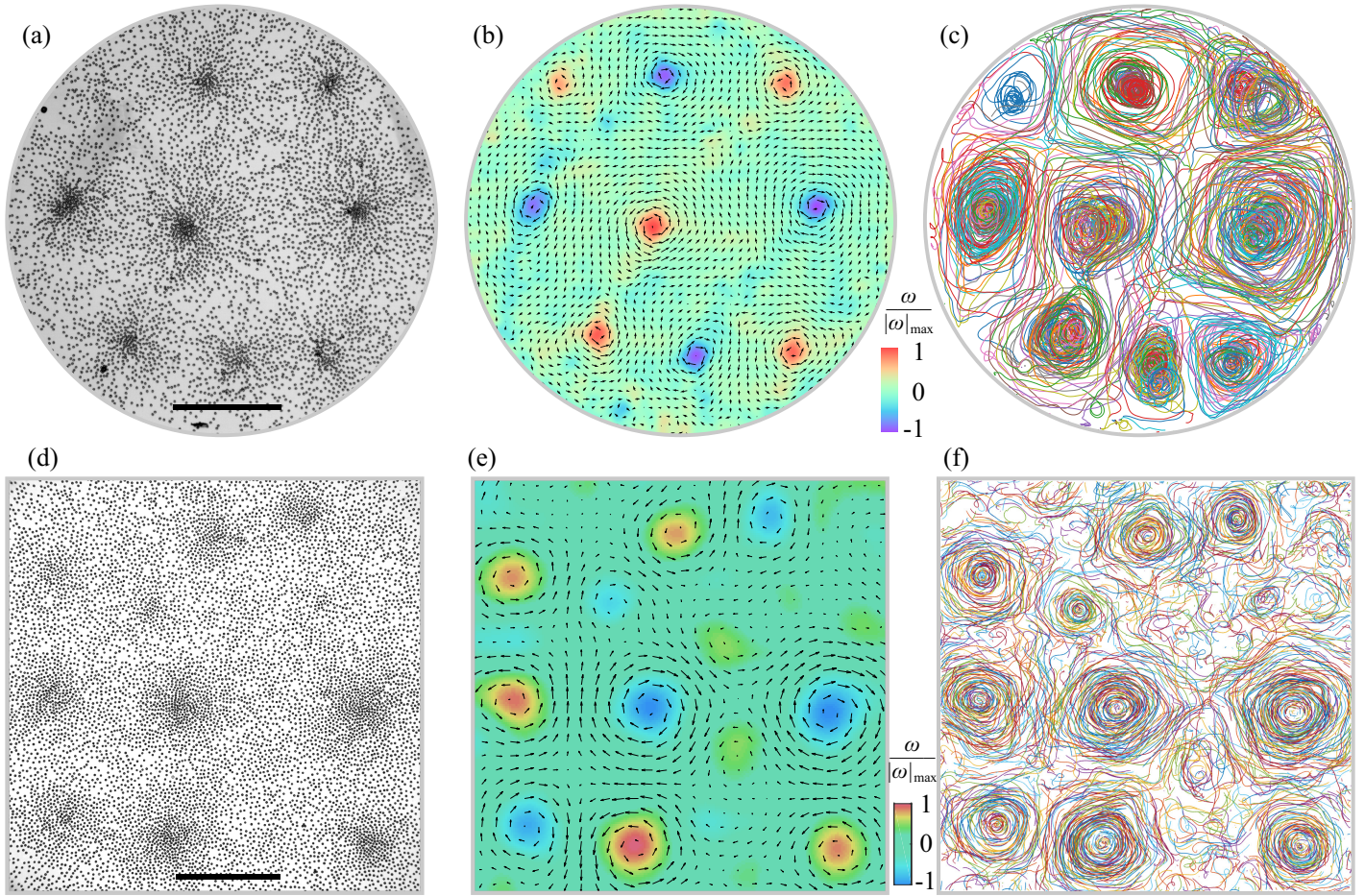


Fig. 2 Emergent multiple vortices in ensembles of shape anisotropic rollers (a-c) and rollers with polarization memory (d-f). (a), Experimental snapshot of multiple vortices spontaneously formed in the ensemble of pear-shaped rollers energized by DC electric field. Vortices rotate either clockwise (CW, blue circle) or counter clockwise (CCW, red circle). The area fraction $\phi = 0.144$. The electric field strength $E = 2.08 \text{ V}/\mu\text{m}$. The scale bar is 0.5 mm. (b), Superimposed velocity (black arrows) and vorticity (background colors) fields of the ensemble shown in (a). (c), Typical particle trajectories of rollers shown in (a). Only 2 % of particle trajectories are shown. (d), Microscopy image of vortices formed by spherical rollers under a pulsed electric field. $E = 2.25 \text{ V}/\mu\text{m}$, $\tau_R = 10 \text{ msec}$, $\tau_T/\tau_{MW} = 3.8$. $\phi = 0.17$. The scale bar is 2 mm. (e), Superimposed velocity (black arrows) and vorticity (background color) fields of the rollers shown in (d). (f), Particle trajectories of rollers shown in (d).

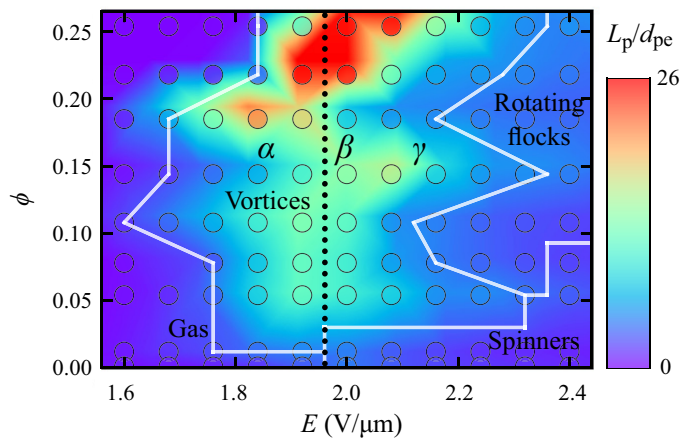


Fig. 3 Persistence lengths of pear-shaped rollers as a function of electric field strength at different area fractions of the active rollers. White curves outline the boundaries between dynamic phases. The black dotted line indicates position of the transition field from α -mode to γ -mode.

port emergence of states with multiple vortices (see Fig. 2). Formation of collective phases in active systems is promoted by velocity alignment interactions facilitated by inelastic particle collisions^{36,37}. In the case of Quincke rollers, both hydrodynamic and electrostatic interactions contribute to the velocity alignment interactions and, as a result, to a buildup of spatial correlations^{13,33}. The electrostatic alignment interactions scale as $\sim (1 - E_q^2/E^2)$ (here E_q is a parameter that depends on the particle and media properties), and the hydrodynamic interactions yield no dependence on the strength of the electric field¹³. For the shape anisotropic Quincke rollers the effect of the electric field on alignment interactions is more complicated since the strength of the field also controls the curvature of rollers' trajectories and the localization of the rollers.

In the case of chiral rollers multiple vortices form in the vicinity of the transition between rolling regimes of the pear-shaped particles³³. As a result, self-organized multiple vortices could form in all three regimes of rolling (α , β or γ modes) giving rise to distinctive vortices with either polar orientational order (with

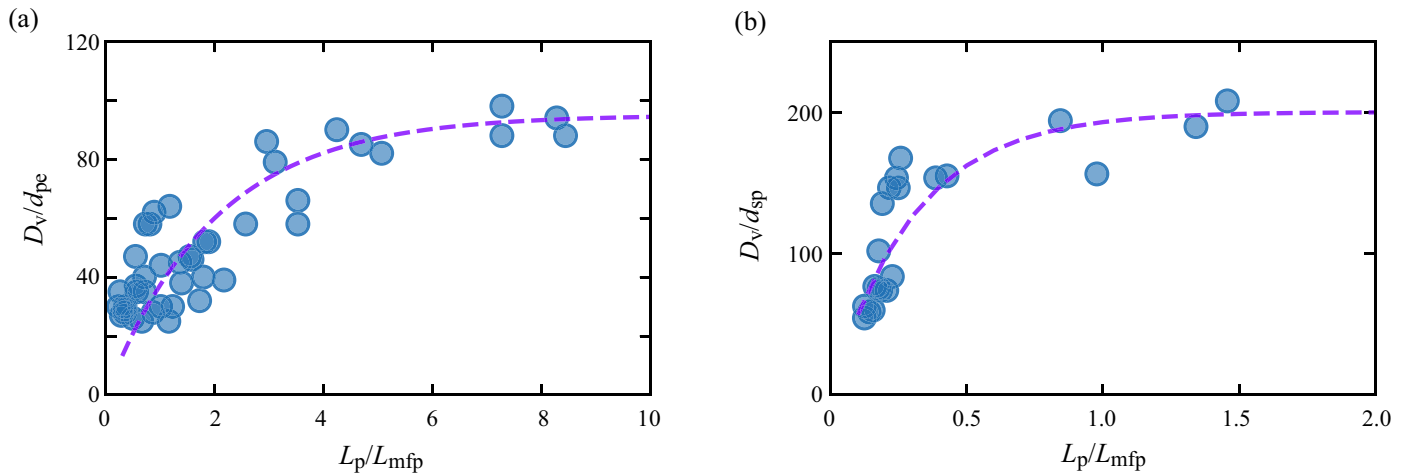


Fig. 4 Control of a characteristic vortex size. (a), Vortex sizes D_v as a function of persistence lengths L_p of pear-shaped rollers under different experimental conditions. Multiple vortices exist in all cases. The vortex size D_v is defined as a second zero crossing in the velocity spatial correlation function of rollers (See Supplementary Figure 4). The length of mean free path L_{mfp} is defined as $L_{mfp} = \pi d / (4\phi)$, where d is a particle size. $\phi \approx 0.05 - 0.25$ for pear-shaped rollers. (b), Variation of a vortex size D_v with the persistence length L_p of spherical rollers for all experiments showing vortex arrays. In all experiments, $\phi \approx 0.15 - 0.18$ for spherical rollers. The dashed curves are fits to a saturating exponential function (see text for details).

all the particles' orientations within the vortex pointing away (α -vortices) or toward (γ -vortices) the eye of the vortex) or nematic order (β -vortices) with both particles' alignments present in a single vortex³³. The direction of each vortex rotation (clockwise or counterclockwise) is spontaneously selected, and vortices with opposite chiralities are simultaneously present in the ensemble in approximately equal ratio. Vortices with the same chirality are usually separated by those with the opposite chirality as demonstrated by the snapshots of typical velocity and vorticity fields shown in Fig. 2b. Once formed, vortices are dynamically stable and localized as illustrated by the trajectories of rollers over time (Fig. 2c). Most rollers have circular trajectories within the vortices, while a small fraction of rollers at the outer rims of the vortices are delocalized.

In the regimes of the collective motion that emerge at elevated area fraction of rollers, the average speed of the particles increases compared to the speed of isolated rollers at the same field strength (see Supplementary Figure 2) owing to the onset of macroscopic flows generated by collective phases (either flocks or vortices) as well as reduced probability of collisions between collectively moving particles. Corresponding persistence length of the rollers, L_p , is also enhanced by a collective motion, see Fig. 3. Among all the phases, the vortices correspond to the longest persistence lengths.

Manipulated by a pulsed electric field, partially correlated spherical rollers form multiple vortices when $2 \leq \tau_T / \tau_{MW} \leq 4$, see Fig. 2d. Similar to the vortex arrays formed by pear-shaped rollers, both vortex chiralities are simultaneously realized with about equal probabilities as illustrated by the velocity and vorticity fields shown in Fig. 2e. While some rollers loosely travel among different vortices, most rollers circulate within a specific vortex over a long time (Fig. 2f). Multiple stable vortices are formed and localized without the confinement from the bound-

ary. The full phase diagram of the emergent patterns is provided in Supplementary Figure 3.

Characteristic size of the vortices in the self-organized multi-vortical state observed in both systems varies with the activity (controlled by the strength of the electric field) and roller area fraction. To track a characteristic size of a vortex we introduce parameter D_v defined as a second zero crossing of the velocity spatial correlation function, $C_s(r) = \langle \langle \mathbf{v}_i(r_0, t) \cdot \mathbf{v}_j(r_0 + r, t) \rangle \rangle_{i,j} / \langle \langle \mathbf{v}_i^2(r_0, t) \rangle \rangle_{i,t}$, where $\mathbf{v}_i(r_0, t)$ and $\mathbf{v}_j(r_0 + r, t)$ are velocities of roller i and j at a relative distance r at a time t ; $\langle \rangle_i$ is an ensemble average; and $\langle \rangle_t$ is the time average (see Supplementary Figure 4). For the case of pear-shaped rollers, D_v is a non-monotonic function of the electric field strength controlling the activity in the system (see insert of Supplementary Figure 4), however all the D_v data obtained at different activity levels and areal roller densities collapse on a single curve when plotted as a function of the corresponding roller persistence length as demonstrated in Fig. 4a. Similar behavior is observed for spherical rollers in a pulsed electric field, see Fig. 4b. The vortex size increases with the persistence length L_p , however as the persistence length of the rollers approaches the average length-scale of the void space between particles (approximately equal to the mean free path $L_{mfp} = \pi d / (4\phi)$), the lattice cannot accommodate larger vortices, and the curve starts to plateau. The observed behavior is well fitted by a simple expression, $D_v = D_0 (1 - \exp(-L_p/L_0))$ shown in the Fig. 4a, b as a dashed curve. Here, D_0 corresponds to a maximum vortex size that is reached at a characteristic persistence length L_0 . For both systems L_0 is of the order of a single mean free path length. With all the data collapsed onto a single curve, the plot suggests that a single parameter, namely L_p , controls both the emergence and corresponding size of the vortices for all different values of $|\nu|$, τ_R , τ_T and ϕ .

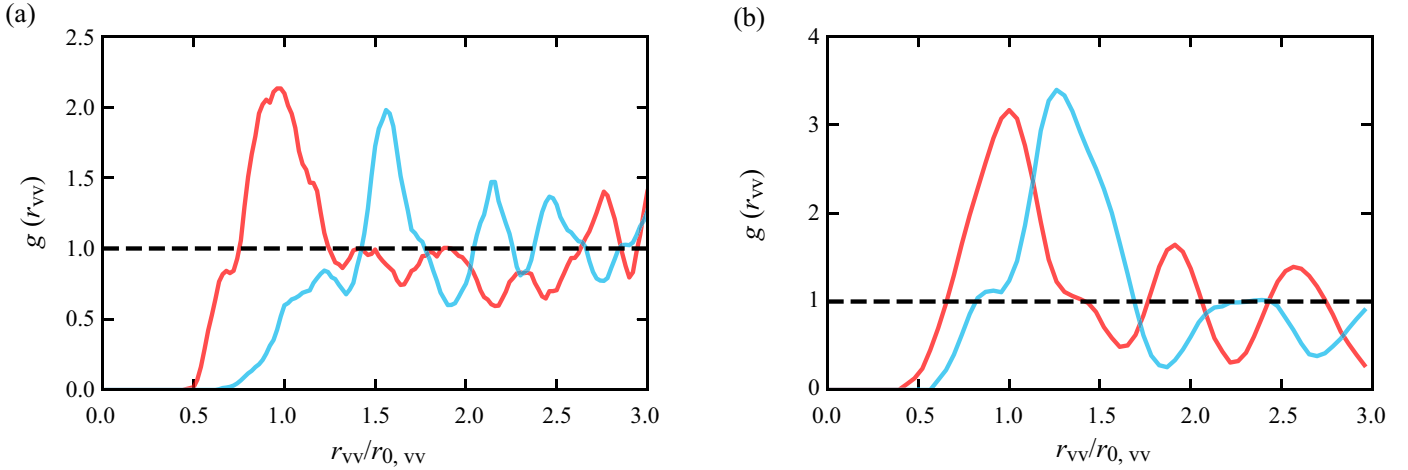


Fig. 5 A quasiantiferromagnetic order of vortex arrays. A pair correlation functions $g(r_{vv})$ of vortices with opposite (red) and same (blue) chiralities formed in the ensemble of (a) pear-shaped rollers, and (b) spherical rollers. The distance between vortices r_{vv} is normalized by the first peak position of $g(r_{vv})$ of vortices with opposite chiralities $r_{0, vv}$.

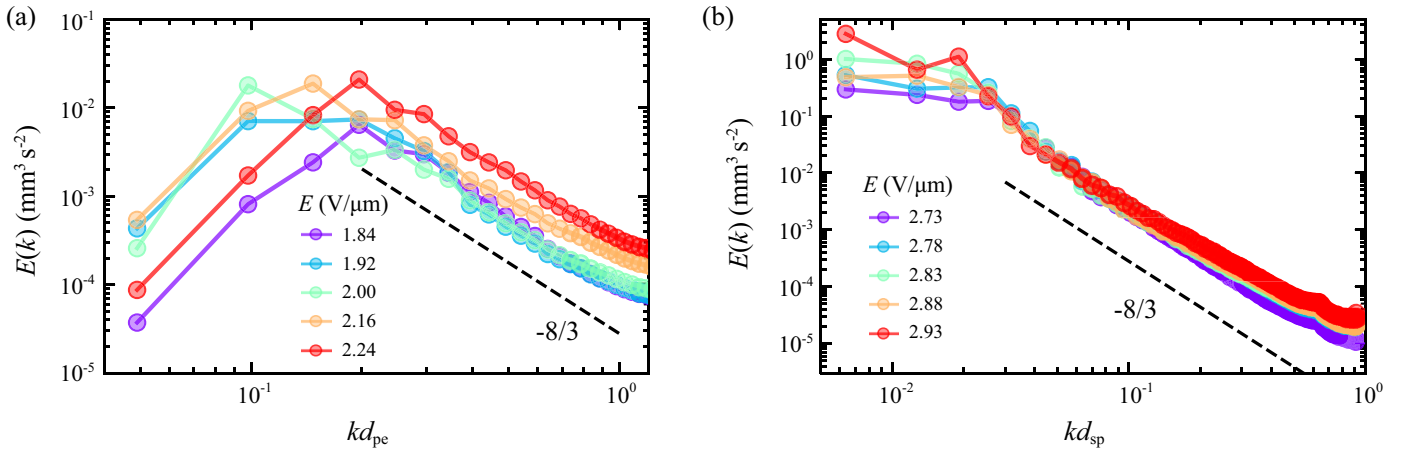


Fig. 6 Velocity field energy spectra of the vortex arrays. Energy spectra of the multivortical velocity field induced in the ensemble of (a) pear-shaped rollers and (b) spherical rollers under pulsed electric field. Both spectra demonstrate inverse energy cascade with characteristic exponent $-8/3$ (black dash lines). In (a) the area fraction is $\phi = 0.144$. In (b), $\tau_R = 7$ ms and $\tau_T/\tau_{MW} = 3.89$, $\phi = 0.17$. Energy spectra of the vortex arrays formed under other combinations of τ_R and τ_T/τ_{MW} show a similar trend.

Regardless of the exact mechanism of the persistence length control used, the system robustly undergoes a transition to a self-organized multi-vortical state in a certain range of the persistence lengths. Spatially localized vortices with characteristic sizes not commanded by the external boundaries further arrange themselves into quasi-antiferromagnetically ordered arrays with respect to the vortex chiralities. As illustrated in the vorticity fields in Fig. 2b, e, same chirality vortices are typically separated by vortices with the opposite chiral state. Although a long-range antiferromagnetic order is missing in both systems, a local antiferromagnetic order can be detected by comparing the pair correlation functions $g(r_{vv})$ of the vortices with same or opposite chiralities shown in Fig. 5. For both systems the first peak positions of $g(r_{vv})$ calculated for same chirality vortices (blue curve) is shifted to larger intervortex distances r_{vv} compared to vortices with opposite chiralities (red curve), indicating the antiferromagnetic nature of a vortex nearest neighborhood. Such ordering minimizes

the particle collisions for rollers in the inter-vortex spaces, eases the shear stresses from vortex generated hydrodynamic flows (see Fig. 2b)), and as a result stabilizes the multi-vortex pattern. Similar quasi-antiferromagnetic ordering of multiple vortices has been also observed in other active matter systems, both in simulations and experiments^{22,29,31,38–40}.

We further analyzed the energy spectrum of the particle flows in both systems in self-organized multivortical states. Typical energy spectra $E(k)$ of the velocity fields as extracted from experiments are shown in Fig. 6. Both spectra resemble that of an inverse energy cascade in classical 2D turbulence⁴¹. Active colloidal ensembles often demonstrate the emergence of meso-scale turbulent motion – so called active turbulence in analogy to the classic macroscopic Kolmogorov-Kraichnan turbulence. However, in contrast to classical systems demonstrating turbulent behavior, active turbulence happens at significantly smaller Reynolds (Re) numbers (often $Re < 1$). While the energy in classic turbulence

cascades from large-scale structures to smaller scales⁴², active particles inject energy at the microscopic level. Unlike the universal $k^{-5/3}$ -decay in large- k part of the energy spectra observed in classical Kolmogorov-Kraichnan 2D turbulence⁴², active turbulence does not produce a universal exponent and different active systems often exhibit dissimilar power-law exponents (with the majority of the active systems, however, exhibiting either $-5/3$ or $-8/3$ behavior)^{20,39,43–46}. Here, both systems of Quincke rollers in multi-vortex state exhibit a consistent slope of $-8/3$ of the energy cascade in the energy spectra regardless of the mechanics of the persistence length control, and in a wide range of control parameters, see Fig. 6.

5 Conclusions

We demonstrate that the collective behavior of the classical spherical Quincke rollers can be significantly enriched by modifying their locomotion pattern through two different methods, namely the shape anisotropy and the polarization memory. Stable long-lived multiple vortices not controlled by a geometrical confinement emerge in such systems of Quincke rollers, and both vortex chiralities (clockwise and counterclockwise) are equally probable. Vortex arrays form in both investigated systems triggered by manipulation of the persistence length of individual rollers. We reveal a direct link between the persistence length and properties of the emergent vortices. We demonstrate that the typical size of localized vortices is related to the persistence length of individual active particles and could be manipulated in-situ. The self-assembled vortices organize into multi-vortical states with a quasi-antiferromagnetic ordering, where identical chirality vortices are separated by those with opposite chiralities. We further demonstrate that both systems share similar energy spectra of the flow velocity fields reminiscent of active turbulent behavior with a characteristic slope of $-8/3$ observed in a wide range of control parameters. Our findings provide insights into the onset of spatiotemporal coherence in active roller systems and suggest a new control knob for manipulation of dynamic self-assembly in active colloidal ensembles.

Conflicts of interest

There are no conflicts to declare.

Acknowledgements

The research of B.Z and A.S has been supported by the U.S. Department of Energy, Office of Science, Basic Energy Sciences, Materials Sciences and Engineering Division. Use of the Center for Nanoscale Materials, an Office of Science user facility, was supported by the U.S. Department of Energy, Office of Science, Office of Basic Energy Sciences, under Contract No. DE-AC02-06CH11357. H.K and P.V have been supported by National Science Foundation award DMR-2004926.

Notes and references

- 1 I. S. Aranson, *Physics-Usppekhi*, 2013, **56**, 79.
- 2 A. Zöttl and H. Stark, *Journal of Physics: Condensed Matter*, 2016, **28**, 253001.
- 3 J. E. Martin and A. Snezhko, *Reports on Progress in Physics*, 2013, **76**, 126601.
- 4 M. C. Marchetti, J.-F. Joanny, S. Ramaswamy, T. B. Liverpool, J. Prost, M. Rao and R. A. Simha, *Reviews of Modern Physics*, 2013, **85**, 1143.
- 5 A. Doostmohammadi, J. Ignés-Mullol, J. M. Yeomans and F. Sagués, *Nature communications*, 2018, **9**, 1–13.
- 6 A. Demortière, A. Snezhko, M. V. Sapozhnikov, N. Becker, T. Proslir and I. S. Aranson, *Nature communications*, 2014, **5**, 1–7.
- 7 F. Ma, S. Wang, D. T. Wu and N. Wu, *Proceedings of the National Academy of Sciences*, 2015, **112**, 6307–6312.
- 8 A. M. Brooks, S. Sabrina and K. J. Bishop, *Proceedings of the national academy of sciences*, 2018, **115**, E1090–E1099.
- 9 Z. Wang, Z. Wang, J. Li, S. T. H. Cheung, C. Tian, S.-H. Kim, G.-R. Yi, E. Ducrot and Y. Wang, *Journal of the American Chemical Society*, 2019, **141**, 14853–14863.
- 10 Y. Alapan, B. Yigit, O. Beker, A. F. Demirörs and M. Sitti, *Nature materials*, 2019, **18**, 1244–1251.
- 11 Z. Wang, Z. Wang, J. Li, C. Tian and Y. Wang, *Nature communications*, 2020, **11**, 1–12.
- 12 A. Snezhko, *Current Opinion in Colloid & Interface Science*, 2016, **21**, 65–75.
- 13 A. Bricard, J.-B. Caussin, N. Desreumaux, O. Dauchot and D. Bartolo, *Nature*, 2013, **503**, 95.
- 14 A. Kaiser, A. Snezhko and I. S. Aranson, *Science advances*, 2017, **3**, e1601469.
- 15 M. Driscoll, B. Delmotte, M. Youssef, S. Sacanna, A. Donev and P. Chaikin, *Nature Physics*, 2017, **13**, 375.
- 16 V. Soni, E. S. Bililign, S. Magkiriadou, S. Sacanna, D. Bartolo, M. J. Shelley and W. T. Irvine, *Nature Physics*, 2019, **15**, 1188–1194.
- 17 G. Kokot and A. Snezhko, *Nature communications*, 2018, **9**, 2344.
- 18 K. Yeo, E. Lushi and P. M. Vlahovska, *Physical review letters*, 2015, **114**, 188301.
- 19 A. Souslov, B. C. Van Zuiden, D. Bartolo and V. Vitelli, *Nature Physics*, 2017, **13**, 1091–1094.
- 20 G. Kokot, S. Das, R. G. Winkler, G. Gompper, I. S. Aranson and A. Snezhko, *Proceedings of the National Academy of Sciences*, 2017, **114**, 12870–12875.
- 21 F. Martinez-Pedrero, E. Navarro-Argemí, A. Ortiz-Ambriz, I. Pagonabarraga and P. Tierno, *Science advances*, 2018, **4**, eaap9379.
- 22 K. Han, G. Kokot, O. Tovkach, A. Glatz, I. S. Aranson and A. Snezhko, *Proceedings of the National Academy of Sciences*, 2020, **117**, 9706–9711.
- 23 G. Quincke, *Annalen der Physik*, 1896, **295**, 417–486.
- 24 A. Tsebers, *Fluid Dynamics*, 1980, **15**, 245–251.
- 25 A. Bricard, J.-B. Caussin, D. Das, C. Savoie, V. Chikkadi, K. Shitara, O. Chepizhko, F. Peruani, D. Saintillan and D. Bartolo, *Nature communications*, 2015, **6**, 7470.
- 26 I. H. Riedel, K. Kruse and J. Howard, *Science*, 2005, **309**, 300–303.

- 27 Y. Sumino, K. H. Nagai, Y. Shitaka, D. Tanaka, K. Yoshikawa, H. Chaté and K. Oiwa, *Nature*, 2012, **483**, 448.
- 28 R. Großmann, P. Romanczuk, M. Bär and L. Schimansky-Geier, *The European Physical Journal Special Topics*, 2015, **224**, 1325–1347.
- 29 H. Wioland, F. G. Woodhouse, J. Dunkel and R. E. Goldstein, *Nature physics*, 2016, **12**, 341–345.
- 30 B. Liebchen and D. Levis, *Physical review letters*, 2017, **119**, 058002.
- 31 D. Nishiguchi, I. S. Aranson, A. Snezhko and A. Sokolov, *Nature communications*, 2018, **9**, 4486.
- 32 H. Karani, G. E. Pradillo and P. M. Vlahovska, *Physical review letters*, 2019, **123**, 208002.
- 33 B. Zhang, A. Sokolov and A. Snezhko, *Nature Communications*, 2020, **11**, 1–9.
- 34 W. Thielicke and E. J. Stamhuis, *Journal of Open Research Software*, 2014, **2**, year.
- 35 D. Allan, T. Caswell, N. Keim and C. van der Wel, *Zenodo*, 2016.
- 36 D. Grossman, I. Aranson and E. B. Jacob, *New Journal of Physics*, 2008, **10**, 023036.
- 37 T. Hanke, C. A. Weber and E. Frey, *Physical Review E*, 2013, **88**, 052309.
- 38 A. Doostmohammadi, M. F. Adamer, S. P. Thampi and J. M. Yeomans, *Nature communications*, 2016, **7**, 10557.
- 39 R. Großmann, P. Romanczuk, M. Bär and L. Schimansky-Geier, *Physical review letters*, 2014, **113**, 258104.
- 40 B. Zhang, B. Hilton, C. Short, A. Souslov and A. Snezhko, *Physical Review Research*, 2020, **2**, 043225.
- 41 G. Boffetta and R. E. Ecke, *Annual Review of Fluid Mechanics*, 2012, **44**, 427–451.
- 42 R. H. Kraichnan and D. Montgomery, *Reports on Progress in Physics*, 1980, **43**, 547.
- 43 J. Dunkel, S. Heidenreich, K. Drescher, H. H. Wensink, M. Bär and R. E. Goldstein, *Physical review letters*, 2013, **110**, 228102.
- 44 H. H. Wensink, J. Dunkel, S. Heidenreich, K. Drescher, R. E. Goldstein, H. Löwen and J. M. Yeomans, *Proceedings of the National Academy of Sciences*, 2012, **109**, 14308–14313.
- 45 G. Li and A. M. Ardekani, *Physical review letters*, 2016, **117**, 118001.
- 46 H. Wensink and H. Löwen, *Journal of Physics: Condensed Matter*, 2012, **24**, 464130.